

RigAnything: Template-Free Autoregressive Rigging for Diverse 3D Assets

Isabella Liu
UC San Diego

Zhan Xu
Adobe Research

Wang Yifan
Adobe Research

Hao Tan
Adobe Research

Zexiang Xu
Hillbot Inc.

Xiaolong Wang
UC San Diego

Hao Su
UC San Diego
Hillbot Inc.

Zifan Shi
Adobe Research



Figure 1: RigAnything is an autoregressive transformer-based approach for automatic rigging. From an arbitrarily posed shape (shown on the left), it can generate a skeleton and skinning weights that adapt seamlessly to the input’s global structure (shown on the right), enabling articulation into new poses.

Abstract

We present *RigAnything*, a novel autoregressive transformer-based model, which makes 3D assets rig-ready by probabilistically generating joints, skeleton topologies, and assigning skinning weights in a template-free manner. Unlike most existing auto-rigging methods, which rely on predefined skeleton template and are limited to specific categories like humanoid, RigAnything approaches the rigging problem in an autoregressive manner, iteratively predicting the next joint based on the global input shape and the previous prediction. While autoregressive models are typically used to generate sequential data, RigAnything extends their application to effectively learn and represent skeletons, which are inherently tree structures. To achieve this, we organize the joints in a breadth-first search (BFS) order, enabling the skeleton to be defined as a sequence of 3D locations and the parent index. Furthermore, our model improves the accuracy of position prediction by leveraging diffusion modeling, ensuring precise and consistent placement of joints within the hierarchy. This formulation allows the autoregressive model to efficiently capture both spatial and hierarchical relationships within the skeleton. Trained end-to-end on both RigNet and Objaverse datasets, RigAnything demonstrates state-of-the-art performance across diverse object types, including humanoids, quadrupeds, marine creatures, insects, and many more, surpassing prior methods in quality, robustness, generalizability, and efficiency. Please check our website for more details: <https://www.liuisabella.com/RigAnything>.

CCS Concepts

• Computing methodologies → Animation; Neural networks.

Keywords

Animation Skeleton, Automatic Rigging, Skinning, Autoregressive Modeling, Transformer-Based Models

1 Introduction

Recent advancements in large-scale 3D asset generation [Hong et al. 2023; Jun and Nichol 2023; Li et al. 2023; Liu et al. 2024b, 2023; Nichol et al. 2022; Shi et al. 2023; Xu et al. 2023] have enabled the creation of highly detailed static shapes. However, since motion is an essential aspect of how humans perceive and interact with the world, there is a growing demand for modeling dynamics to create lifelike and interactive assets [Liu et al. 2024a]. While some approaches leverage text-based [Bahmani et al. 2024; Singer et al. 2023; Zhao et al. 2023] or video-guided [Ren et al. 2023; Yin et al. 2023] control to animate objects, these methods often fall short in providing the precision and flexibility required by artists to fully realize their creative visions. Rigging, in contrast, offer a robust and artist-friendly framework for animation, enabling fine-grained control over degree of freedom and range of motion. Our work addresses this need by presenting a systematic approach to automating rigging, advancing the state of the art in articulable asset generation.

Auto-rigging has long been a challenging research problem in computer graphics [Baran and Popović 2007; Chu et al. 2024; Guo et al. 2024; Li et al. 2021; Xu et al. 2020]. Table 1 provides a concise

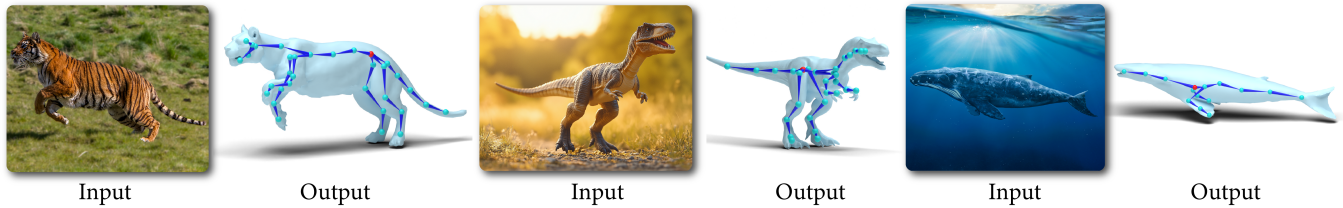


Figure 2: Skeleton generation on shapes obtained from real images, demonstrating that our method generalizes well to real data. Fig. 7 presents additional real results.

summary of state-of-the-art methods in this domain. Most existing approaches depend on predefined skeleton templates [Baran and Popović 2007; Chu et al. 2024; Guo et al. 2024; Li et al. 2021], which limit their applicability to specific categories, such as humanoid characters (Tab. 1). To overcome template reliance, RigNet [Xu et al. 2020] employs non-differentiable operators, including clustering for joint position acquisition and a minimum spanning tree for topology construction. However, this approach requires approximately two minutes to rig a single object and is further constrained to operate only on objects in rest poses.

In this work, we propose a transformer-based autoregressive model, termed **RigAnything**, to make any 3D asset "rig-ready". The autoregressive model probabilistically "grows" the skeleton from the root joint in a sequential manner; Skinning weights for any surface sample are then inferred by holistically considering all the joints.

Specifically, we represent the tree-structured skeleton as a sequence by ordering the joints in a breadth-first search (BFS) order, where each joint is defined by a 3D position and a parent index. This autoregressive formulation is particularly suited for skeleton prediction, as it addresses the inherent ambiguity in joint configurations by representing them as a probabilistic distribution. Additionally, by sequentially generating joints and connections without relying on a predefined template, the model supports arbitrary skeleton structures and varying numbers of joints, enabling broad generalization across diverse object categories. Furthermore, while autoregressive models are traditionally designed to handle discrete values [Brown et al. 2020; Radford et al. 2019; Waswani et al. 2017], inspired by recent work utilizing autoregressive models for image generation [Li et al. 2024], we adopt a diffusion sampling process to predict the continuously valued joint positions, resulting in superior accuracy. Given the predicted skeleton, we infer the skinning weights by a pair-wise computation. We employ transformer blocks throughout the model to comprehensively capture the global shape structure, as well as the interdependence among all joints and their associated surface points.

We train our model end-to-end on both the RigNet dataset [Xu et al. 2020] and a curated subset of high-quality animatable assets from the Objaverse dataset [Deitke et al. 2023]. We rigorously filter the Objaverse dataset and select 9686 high-quality rigged shapes, which enrich the dataset for research in this direction. The input shapes are further augmented with random pose variations to enhance robustness. Our training data encompasses a wide range of object types, including bipedal, quadrupedal, avian, marine, insectoid, and manipulable rigid objects, as well as a diverse set of initial poses. This extensive scale and diversity of training data

Table 1: Feature comparison with other Auto-Rigging tools.

| Methods | Humanoid | Non-Humanoid | Template-Free | Arbitrary Pose | Rigging Time |
|------------------------------------|----------|--------------|---------------|----------------|--------------|
| TARig [Ma and Zhang 2023] | ✓ | ✗ | ✗ | ✗ | ~40s |
| Pinocchio [Baran and Popović 2007] | ✓ | ✓ | ✗ | ✗ | ~40s |
| RigNet [Xu et al. 2020] | ✓ | ✓ | ✓ | ✗ | ~120s |
| RigAnything (Ours) | ✓ | ✓ | ✓ | ✓ | ~2s |

surpasses all prior work, playing a critical role in achieving broad generalizability across shape categories and configurations.

Extensive experiments demonstrate that RigAnything achieves state-of-the-art performance in the auto-rigging task, as demonstrated in Fig. 1, Fig. 2 and Fig. 5, surpassing prior methods in quality, robustness, generalizability, and efficiency. By automating rigging for diverse 3D assets, our method advances the vision of fully interactive 3D environments and scalable 3D content creation, empowering artists and developers with a powerful, efficient tool.

2 Related Work

2.1 Automatic Rigging

Rigging is a fundamental technique for animation in computer graphics. Traditional automatic rigging methods, such as Pinocchio [Baran and Popović 2007], rely on predefined skeletons and optimize their variations to fit a range of characters, with skinning weights determined by analyzing vertex-bone deformation relationships. However, the optimization process is computationally expensive and diminishes the generalizability. Recent advances in deep learning have improved the quality and adaptability of rigging. TARig [Ma and Zhang 2023] utilizes a template with adaptive joints and a boneflow field to generate skeletons and skinning weights for humanoid characters. Li's *et al.* [Li et al. 2021] leverages a predefined skeleton template for characters to learn rigging and proposes neural blend shape to enhance deformation quality. However, these methods are confined to humanoid characters in standard poses and rely heavily on predefined templates, limiting their robustness and generalization to diverse objects, poses, and skeleton topologies.

Differently, RigNet [Xu et al. 2020] use a combination of regression and adaptive clustering to handle the diverse number of joints and employs a deep neural network for connectivity prediction to allow various topologies without templates or assumptions about shape classes and structures. However, it lacks the robustness and efficiency due to its model design, which is not end-to-end trainable with clustering and Minimum Spanning Tree operations. Make-it-Animatable [Guo et al. 2024] and HumanRig [Chu et al. 2024] are works developed concurrently with ours. They also focus solely on

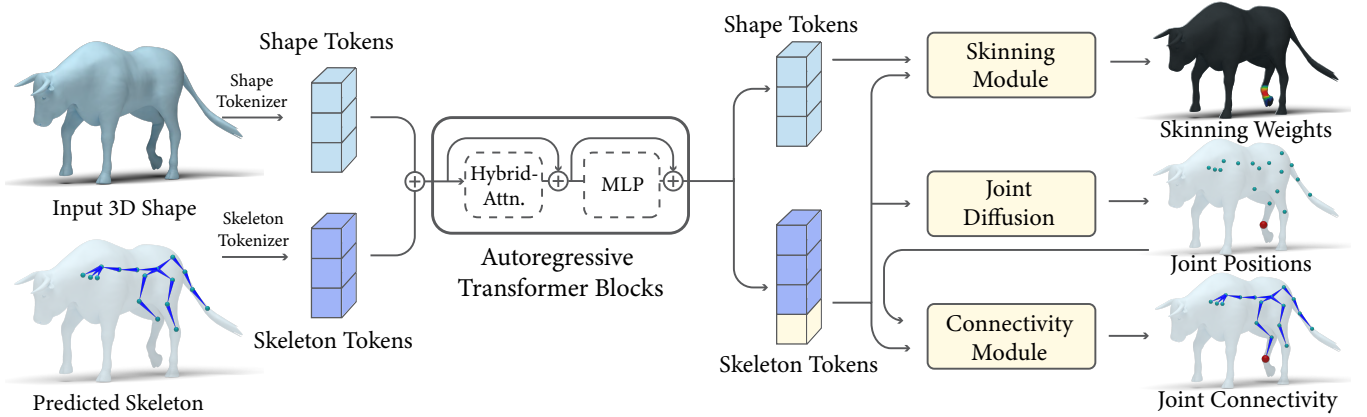


Figure 3: Pipeline of our method: The input shape and the previously predicted skeleton sequence are tokenized using two separate tokenizers. These tokens are processed through a chain of autoregressive transformer blocks with a hybrid attention mask. Shape tokens perform self-attention to capture global geometric information, while skeleton tokens attend to all shape tokens and use causal attention within themselves to maintain the autoregressive generation process. After the transformer blocks, a skinning module decodes shape tokens into skinning weights, a joint diffusion module samples the next joint position, and a connectivity module predicts the next joint’s connection to its preceding joint conditioned on the sampled next joint position from joint diffusion module.

humanoid characters and rely on template skeletons, restricting their adaptability to more diverse data categories. In contrast, our method eliminates the need for templates and avoids assumptions about skeleton topology, achieving greater generalizability and robustness for diverse object types in a feed-forward manner.

2.2 Autoregressive Models for 3D

Autoregressive models are a powerful class of probabilistic models widely applied across domains such as natural language processing [Achiam et al. 2023; Brown et al. 2020; Radford et al. 2019] and computer vision [Chen et al. 2020; Esser et al. 2021; Li et al. 2024; Parmar et al. 2018]. In 3D tasks, autoregressive models have also demonstrated remarkable potential in areas like shape generation [Cheng et al. 2022; Ibing et al. 2023; Mittal et al. 2022; Qian et al. 2024; Yan et al. 2022] and motion generation [Han et al. 2024; Rempe et al. 2021; Zhang et al. 2023]. In 3D shape generation, methods mostly focus on designing effective representations for autoregressive modeling. ShapeFormer [Yan et al. 2022] introduces a sparse representation that quantizes non-empty voxel grids in a predefined order. AutoSDF [Mittal et al. 2022] takes a different approach by modeling the entire space and using randomized sampling orders to enable non-sequential modeling. Octree Transformer [Ibing et al. 2023] introduce octree-based hierarchical shape representations with adaptive compression, significantly reducing sequence lengths. Cheng *et al.* [Cheng et al. 2022] decompose point clouds into semantically aligned sequences. Argus3D [Qian et al. 2024] utilizes discrete representation learning on a latent vector and scales up the model to improve the quality and versatility of 3D generation. Similarly, autoregressive models have advanced 3D motion generation. T2M-GPT [Zhang et al. 2023] uses motion VQ-VAE and textural descriptions for human motion generation. HuMoR [Rempe et al. 2021] proposes hierarchical latent variables for realistic motion synthesis. AMD [Han et al. 2024] presents an autoregressive model that iteratively generates complex 3D human motions from long

textual descriptions. In this paper, we pioneer the application of autoregressive models to the task of automatic rigging, marking a significant advancement in this domain.

3 Method

Our goal is to transform a given 3D shape into an animatable asset by generating a plausible skeleton and predicting the corresponding skinning weights. These enable the 3D asset to be articulated under joint transformations using Linear Blend Skinning (LBS). In this section, we first introduce our novel autoregressive model for skeleton generation in Sec. 3.1, followed by our approach to skinning weight prediction in Sec. 3.2, and conclude with a detailed description of the model architecture in Sec. 3.3.

3.1 Autoregressive Skeleton Prediction

Autoregressive Modeling. The key component of our method is an autoregressive model for the skeleton prediction to address the ambiguity of skeleton structures and eliminates the need for predefined templates. To convert the tree-structured skeleton to a sequence that can be effectively processed by the autoregressive model, we adopt the breadth-first search order (BFS) to serialize the skeleton to a list:

$$\mathcal{J} = [(j_1, p_1), (j_2, p_2), \dots, (j_K, p_K)], \quad (1)$$

where $j_k \in \mathbb{R}^3$ and $p_k \in \{1, \dots, K\}$ denote the 3D position and the parent index of the k -th joint respectively. As we adopt the BFS order, $p_k < k$ and the first element (j_1, p_1) always represents the root joint. The order of joints at the same BFS depth level is non-deterministic. To resolve this ambiguity, we randomly sample the order during training and uses generative modeling to cover the uncertainty.

Given an input shape \mathcal{S} represented by L sampled points, we factorize the joint probability of skeleton by the chain rule:

$$P(\mathcal{J} | \mathcal{S}) = \prod_{k=1}^K P(j_k, p_k | \mathcal{J}_{1:k-1}, \mathcal{S}).$$

where $\mathcal{J}_{1:k}$ is the shorthand for the sublist of \mathcal{J} up to the k -th element.

The autoregressive model is tasked to iteratively predict the conditional distribution of each joint position j_k and parent index p_k , formulated as

$$P(j_k, p_k | \mathcal{J}_{1:k-1}, \mathcal{S}) = P(j_k | \mathcal{J}_{1:k-1}, \mathcal{S}) P(p_k | j_k, \mathcal{J}_{1:k-1}, \mathcal{S}).$$

Instead of directly modeling in the original joint space, we map all previously predicted joints and their corresponding parents into a higher-dimensional token space to enhance the model’s expressive capacity. This token space effectively represents the evolving state of the skeleton, capturing its structural and hierarchical information as new joints and connections are incrementally added. Similarly, a sequence of shape tokens is extracted to encapsulate the global structure of the input shape, providing consistent contextual information throughout the modeling process. Denoting the skeleton tokens as $T_{1:k-1} \in \mathbb{R}^{(k-1) \times d}$ and the shape token as $H \in \mathbb{R}^{L \times d}$, the prediction targets are reformulated as:

$$P(j_k | T_{1:k-1}, H) \quad \text{and} \quad P(p_i | j_i, T_{1:k-1}, H). \quad (2)$$

The extraction of the skeleton token T and shape token H are detailed in Sec. 3.3.

Joint Prediction with Diffusion Model. To predict the next joint position, which is continuously valued, we address the limitation that most autoregressive models are traditionally designed for discrete outputs, making them less effective for continuous-valued tasks. Inspired by recent autoregressive image generation models [Li et al. 2024], we adopt a diffusion sampling process [Dhariwal and Nichol 2021; Ho et al. 2020; Nichol and Dhariwal 2021] to handle the continuous nature of joint positions. Diffusion models are particularly suited for this task because they iteratively refine samples, effectively resolving the structural ambiguities inherent in skeleton tree representations. For readability, we drop the current joint index k in the following part.

Forward Diffusion Process: The forward process gradually adds Gaussian noise to the ground-truth joint j^0 over M time steps, producing increasingly noisy versions j^m . This is formulated as:

$$j^m = \sqrt{\bar{\alpha}_m} j^0 + \sqrt{1 - \bar{\alpha}_m} \epsilon,$$

where $\epsilon \sim \mathcal{N}(\mathbf{0}, \mathbf{I})$ is Gaussian noise, and $\bar{\alpha}_m = \prod_{s=1}^m \alpha_s$ defines a noise schedule.

Training Objective: We train a noise estimator ϵ_θ , conditioned on the diffusion time step m and the context $Z \in \mathbb{R}^{(L+k-1) \times d}$, where

$$Z = \text{TransformerBlocks}(T_{1:k-1}, H), \quad (3)$$

capturing both the evolving skeleton state and the input shape. Here, Tr refers to the transformer blocks that are detailed in Sec. 3.3. The model takes the noisy joint j^m as input and predicts the added noise ϵ . The training objective is defined as:

$$\mathcal{L}_{\text{joint}}(Z, j^0) = \mathbb{E}_{\epsilon, m} [\|\epsilon - \epsilon_\theta(j^m | m, Z)\|^2]. \quad (4)$$

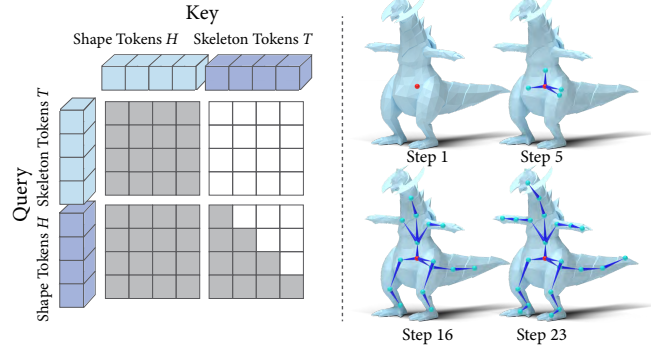


Figure 4: (Left) Hybrid attention mask: Shape tokens use full self-attention, while skeleton tokens attend to shape tokens and apply causal masking among themselves. (Right) The skeleton sequence is autoregressively generated during inference.

Reverse Diffusion Process: At inference time, the reverse process iteratively removes noise, sampling the next joint position $j^0 \sim p_\theta(j^0 | Z)$. Starting from a Gaussian sample $j^M \sim \mathcal{N}(\mathbf{0}, \mathbf{I})$, the reverse process is defined as:

$$j^{m-1} = \frac{1}{\sqrt{\alpha_m}} \left(j^m - \frac{1 - \alpha_m}{\sqrt{1 - \bar{\alpha}_m}} \epsilon_\theta(j^m | m, Z) \right) + \sigma_m \delta, \quad (5)$$

where $\delta \sim \mathcal{N}(\mathbf{0}, \mathbf{I})$ is Gaussian noise, and σ_m denotes the noise level at step m . The final output j^0 represents the predicted joint position.

Connectivity Prediction. After we sample the next joint position $j_k \in \mathbb{R}^3$ from the diffusion module described earlier, we aim to predict how this newly sampled joint j_k connects to its ancestor joints. We first update the context Z_k with the sampled joint j_k through a fusing module F:

$$Z'_k = F(Z_k, j_k, \gamma(k)), \quad (6)$$

where $\gamma(k) \in \mathbb{R}^d$ is a positional embedding signaling the current joint index.

Next, a connectivity module C takes Z'_k and each individual predicted skeleton token T_i ($i < k$) (detailed in Sec. 3.3) produce the parent joint probability,

$$\mathbf{q}_k = \text{Softmax}\left([\text{C}(Z'_k, T_i)]_{i=1}^{k-1}\right). \quad (7)$$

The connectivity is supervised with the binary cross-entropy loss,

$$\mathcal{L}_{\text{connect}} = - \sum_{i=1}^{k-1} [\hat{y}_{k,i} \log(q_{k,i}) + (1 - \hat{y}_{k,i}) \log(1 - q_{k,i})], \quad (8)$$

where $q_{k,i}$ is the i -th element in \mathbf{q}_k and $\hat{y}_{k,i} \in \{0, 1\}$ is the ground-truth label indicating whether joint j_k is connected to joint j_i .

During training, the ground-truth next joint position j_k is fed into the network for connectivity prediction, while during the inference time, j_k is sampled from the joint diffusion module and subsequently passed to the connectivity network.

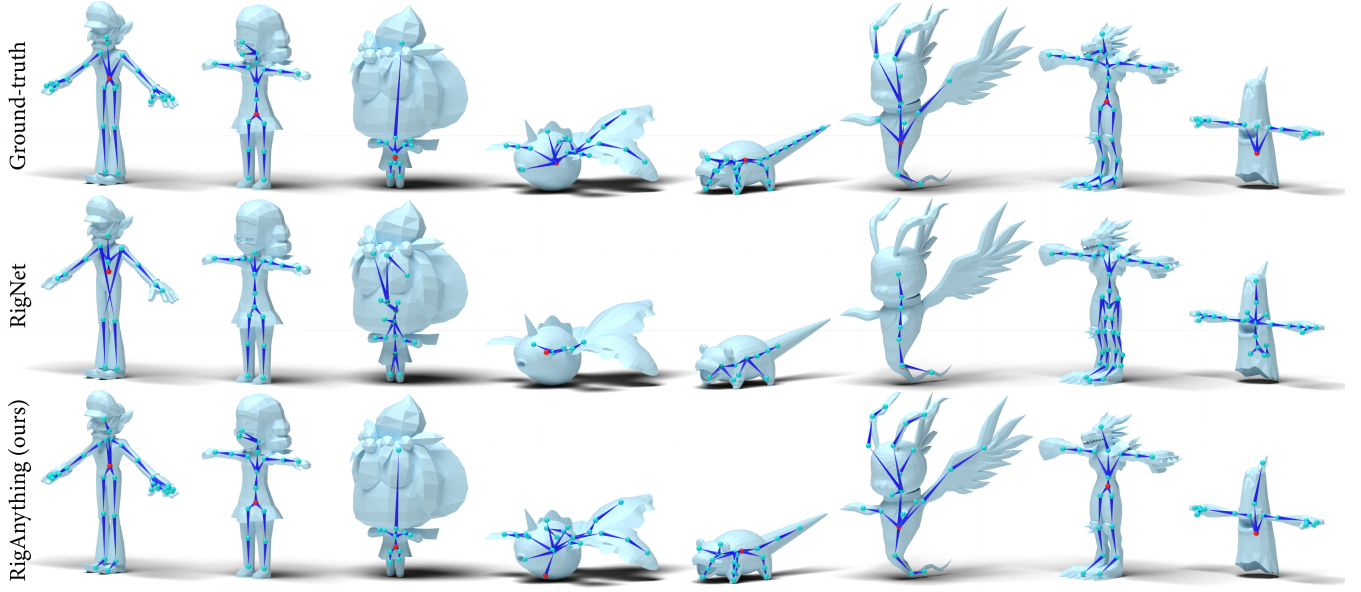


Figure 5: Comparison of reconstructed skeletons between our method, RigNet, and ground truth. Our method generates more accurate and satisfying skeletons across diverse shape categories. While RigNet tends to produce excessive joints and struggles with uncommon shapes like characters with tails or wings. Our approach generates a reasonable number of joints and aligns the skeletons closely with the underlying shapes. Note that RigNet supports only rest poses, so all evaluations are conducted on rest-posed objects for fairness.

3.2 Skinning Prediction

Skinning weights are described by a matrix $W \in \mathbb{R}^{L \times K}$, where each element w_{lk} indicates the influence of the k -th joint on the l -th surface point in \mathcal{S} . The weight vector $\mathbf{w}_l \in \mathbb{R}^K$ for each surface point must satisfy the following constraints: $\sum_{k=1}^K w_{lk} = 1$ and $w_{lk} \geq 0$ for all k .

To compute the skinning weight \mathbf{w}_l for each surface point $s_l \in \mathcal{S}$, a skinning prediction module G takes as input the shape token $H_{s_l} \in \mathbb{R}^d$ for point s_l , along with the skeleton token T_k for each joint j_k ($k \leq K$). The module outputs a predicted influence score for each joint j_k on s_l . The final skinning weight \mathbf{w}_l is computed using the softmax function:

$$\mathbf{w}_l = \text{Softmax}\left(\left[G(H_{s_l}, T_k)\right]_{k=1}^K\right), \quad (9)$$

We train this module by minimizing a weighted cross-entropy loss, where the ground-truth skinning weight $\hat{\mathbf{w}}_l$ serves as the weighting factor, which can be written as.

$$\mathcal{L}_{\text{skinning}} = \frac{1}{L} \sum_{l=1}^L \left(- \sum_{k=1}^K \hat{w}_{l,k} \log(w_{l,k}) \right). \quad (10)$$

This formulation encourages the model to produce higher probabilities for joints with larger ground-truth skinning weights, thereby aligning the learned distribution with the correct influences for each point.

3.3 Autoregressive Transformer Architecture

Our autoregressive modeling is anchored on a transformer-based architecture, which outputs the shape tokens $H \in \mathbb{R}^{L \times d}$ and skeleton tokens $T_{1:k} \in \mathbb{R}^{k \times d}$ ($0 < k \leq K$) that serve as conditional inputs for the autoregressive modeling for skeleton prediction (Sec. 3.1) and skinning prediction (Sec. 3.2). The extraction of these tokens involve two steps: first, referred as the “tokenization” step, an initial shape token and skeleton tokens are lifted from the raw input, this step produces a higher dimensional vector that has sufficient capacity in preparation to capture richer information in the further processing steps in the transformer; subsequently, the transformer process these tokens through a series of attention blocks with carefully crafted attention masking to obtain the final shape and skeleton tokens, which are finally used as inputs to the skeleton and skinning prediction modules in Sec. 3.1 and Sec. 3.2.

Tokenization. For the shape data, we sample a set of L surface points $S \in \mathbb{R}^{L \times 3}$ and concatenate them with their corresponding normals $N \in \mathbb{R}^{L \times 3}$, forming a sequence of L tokens each with 6 dimensions. These tokens are then passed through MLP layers to a d -dimensional space. Formally, the shape tokens $H \in \mathbb{R}^{L \times d}$ can be written as

$$H = \text{MLP}(\text{Concat}(S, N)). \quad (11)$$

For the skeleton data, we first apply MLPs to project each joint position j_k and its corresponding parent joint position j_{p_k} into a d -dimensional space. These features are then concatenated with positional embeddings, which encode the index of each joint within the sequence. Finally, the concatenated features are processed through MLP layers to obtain the per-joint skeleton tokens. These steps can

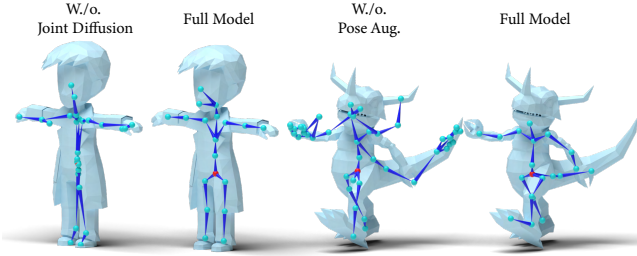


Figure 6: (Left) Joint diffusion modeling prevents joint collapse to mean positions, capturing diverse modalities. (Right) Pose augmentation improves generalization to unseen poses, ensuring well-aligned skeletons and avoiding excessive joints.

be expressed formally as

$$T_k = \text{MLP}\left(\text{Concat}(\text{MLP}(j_k), \gamma(k), \text{MLP}(j_{p_k}), \gamma(p_k))\right). \quad (12)$$

The skeleton token $T_{1:K} \in \mathbb{R}^{K \times d}$ is a sequence of individual per-joint tokens in BFS-order.

Processing Tokens with Transformer. The extracted shape tokens H and predicted skeleton tokens $T_{1:k-1}$ are concatenated and then treated as $L + (k - 1)$ individual tokens. These are then passed through a chain of transformer blocks, in which multi-head self-attention mechanisms ensure that the skeleton tokens and the shape tokens are aware of each other’s features, enabling the model to capture rich global information and interdependencies between the shape context and the evolving skeleton structure. We propose a hybrid attention mechanism that applies different attention patterns to shape and skeleton tokens. As shown in the left part of Fig. 4, shape tokens attend to each other via full self-attention to capture global geometric context. For skeleton tokens, we first allow them to attend to all shape tokens to incorporate shape information, and then apply causal attention [Radford et al. 2019; Waswani et al. 2017] among the skeleton tokens so that each token only attends to its preceding tokens in the sequence. This ensures the autoregressive property required for skeleton sequential generation.

The output of the last transformer block Z_k will be served as the condition in the diffusion model for joint j_k sampling as introduced in Sec. 3.1.

4 Experiments

4.1 Implementation Details

Our input point cloud consists of 1024 points, with the maximum number of joints per sample set to 64. The point cloud and joint tokenizers are implemented as two-layer MLPs with hidden dimensions of 512 and 1024. For both parent and skinning prediction modules, we employ two-layer MLPs with hidden dimensions of 1024.

The implemented transformer consists of 12 layers with a hidden dimension of 1024. Following the implementation in [Zhang et al. 2025], each transformer block incorporates a multi-head self-attention layer with 16 heads and a two-layered MLP with a hidden dimension of 4096 and a GeLU activation. We employ Pre-Layer Normalization, Layer Normalization (LN), and residual connections

consistent with the reference implementation. During training, we employ a hybrid attention masking strategy: shape tokens perform self-attention to effectively capture geometric information, while skeleton tokens use causal attention, attending only to their ancestor skeleton tokens within the sequence to facilitate auto-regressive generation. Additionally, skeleton tokens attend to all shape tokens. During inference, the network processes shape tokens as input and generates skeleton tokens in an auto-regressive manner.

The joint diffusion process follows [Li et al. 2024; Nichol and Dhariwal 2021], which has a cosine noise scheduler with 1000 training steps and 300 resampling steps during inference. The denoising MLP is conditioned on the transformer-outputted joint tokens, where these tokens are incorporated into the noise scheduler’s time embedding through AdaLN [Peebles and Xie 2023] within the Layer Normalization layers.

The fusing module is a two-layer MLP with an input size of 3072 and hidden dimensions of 2048 and 1024. During inference, after obtaining the next joint position via diffusion sampling, a shape tokenizer generates a latent shape token (dimension 1024), which is concatenated with previous context tokens (dimension 1024) and positional embeddings. The fusing module’s output serves as the updated context for connectivity and skinning prediction. Both the connectivity and skinning modules share a similar architecture with the fusing module, except their input size is 2048.

4.2 Dataset

We utilize both the RigNet dataset [Xu et al. 2020] and the Objaverse dataset [Deitke et al. 2023]. The RigNet dataset contains 2,354 high-quality 3D models with ground-truth skeleton and skinning annotations. The Objaverse dataset offers a large collection of 3D models with varying rigging quality. To ensure data reliability, we filtered out 9,686 models with consistent and accurate skeleton and skinning information. Our dataset spans a diverse range of categories, including bipedal, quadrupedal, avian, marine, insectoid, and manipulable rigid objects. For each model, we sample point clouds and face normals from the mesh surface.

During training, we perform online augmentation to the input data by randomly deforming the input point clouds using the ground-truth skeleton and skinning. As shown in our ablation study in Sec. 4.4 and Fig. 6, this augmentation strengthens our method’s ability to generalize to objects in different poses.

4.3 Evaluation and Baseline Comparisons

4.3.1 Skeleton Prediction. We provide qualitative visualizations of the reconstructed skeletons in comparison with the ground truth and RigNet in Fig. 5. Our method demonstrates superior performance, producing more accurate and satisfying skeletons across various shape categories. In contrast, RigNet [Xu et al. 2020] struggles to recover reasonable skeletons for less common shapes, such as characters with tails or wings, and frequently generates an excessive number of joints. In comparison, our method generates a reasonable number of joints, with the reconstructed skeletons well-aligned to the underlying shape, ensuring better structural consistency and fidelity.

To quantitatively evaluate the performance of skeleton prediction, we measure the similarity between the predicted skeletons

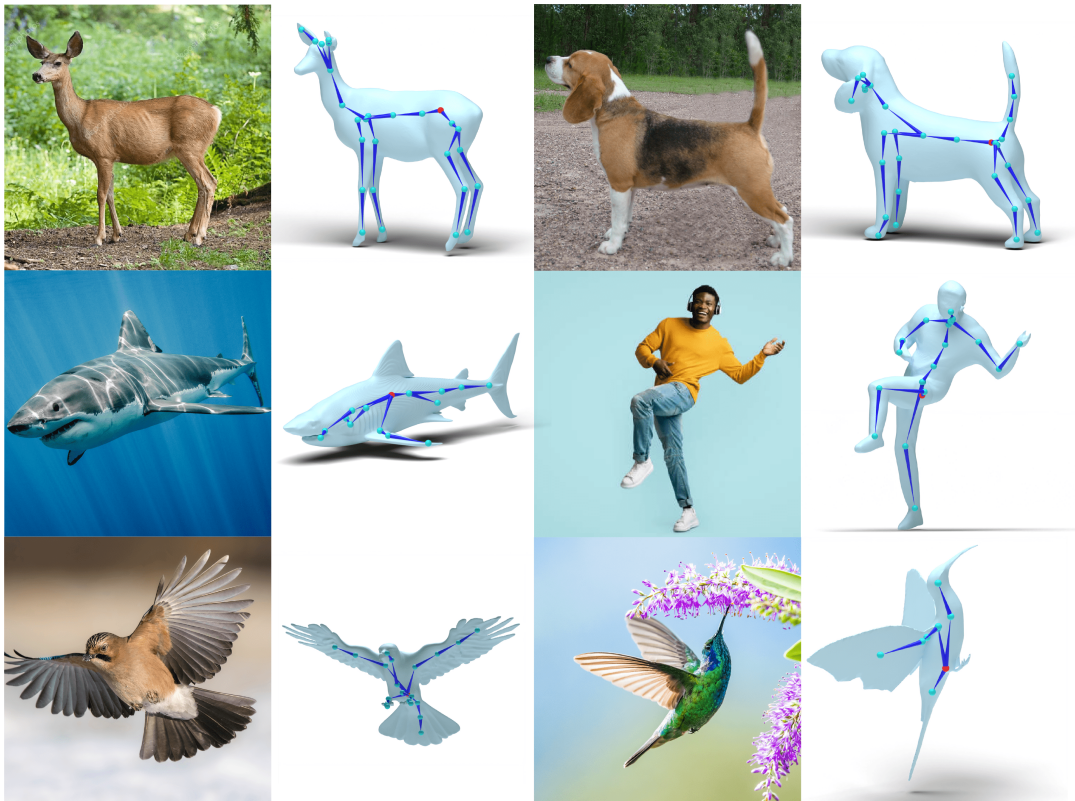


Figure 7: Skeleton results on shapes from real casual images. We use off-the-shelf image-to-3D model pipeline [Liu et al. 2024c] to generate the shapes from real images and apply RigAnything to predict their skeletons.

and the ground truth on the RigNet dataset using multiple metrics: Intersection over Union (IoU), Precision, and Recall for bone matching, as well as Chamfer distances for joints (CD-J2J), bone line segments (CD-B2B), and joint-to-bone line segments (CD-J2B). Table 2 presents a comparison with Pinocchio [Baran and Popović 2007] and RigNet [Xu et al. 2020] across these metrics. The results show that our method significantly outperforms the baselines, producing skeletons that align more closely with the ground truth.

Table 2: Quantitative comparison of skeleton prediction on the RigNet dataset. Our predicted skeletons aligns better with the ground truth.

| | IoU \uparrow | Prec. \uparrow | Rec. \uparrow | CD-J2J \downarrow | CD-J2B \downarrow | CD-B2B \downarrow |
|---------------------------|----------------|------------------|-----------------|---------------------|---------------------|---------------------|
| Pinocchio | 0.365 | 0.387 | 0.359 | 0.072 | 0.055 | 0.047 |
| RigNet | 0.616 | 0.676 | 0.589 | 0.039 | 0.024 | 0.022 |
| RigAnything (Ours) | 0.765 | 0.786 | 0.765 | 0.033 | 0.034 | 0.019 |

4.3.2 *Connectivity Prediction.* We evaluate the connectivity prediction performance when the given joints are from ground truth instead of prediction. We measure the binary classification accuracy (Class. Acc.) for assessing joint pair connections, as well as the CD-B2B and edit distance (ED), which measure the geometric and

topological difference between the predicted and reference skeletons. As shown in Table 3, our method significantly outperforms RigNet across all metrics.

Table 3: Connectivity prediction performance comparison on the RigNet dataset. Our method significantly outperforms RigNet across all metrics.

| | Class. Acc. \uparrow | CD-B2B \uparrow | ED \downarrow |
|---------------------------|------------------------|-------------------|-----------------|
| RigNet | 0.837 | 0.001 | 2.4 |
| RigAnything (Ours) | 0.962 | 0.001 | 2.3 |

4.3.3 *Skinning Prediction.* For skinning prediction performance, we provide a qualitative comparison of our method with RigNet and Blender’s built-in automatic skinning weight calculation, which assigns weights based on the shortest Euclidean distance between mesh vertices and bones in the armature. For a fair comparison, the ground truth skeleton is provided during skinning weight inference. As shown in Fig. 9, our method produces more accurate and consistent skinning weights. In challenging cases where two areas are close in Euclidean space but have a large geodesic distance, our method successfully differentiates these parts and generates consistent skinning weights, whereas the baselines fail.

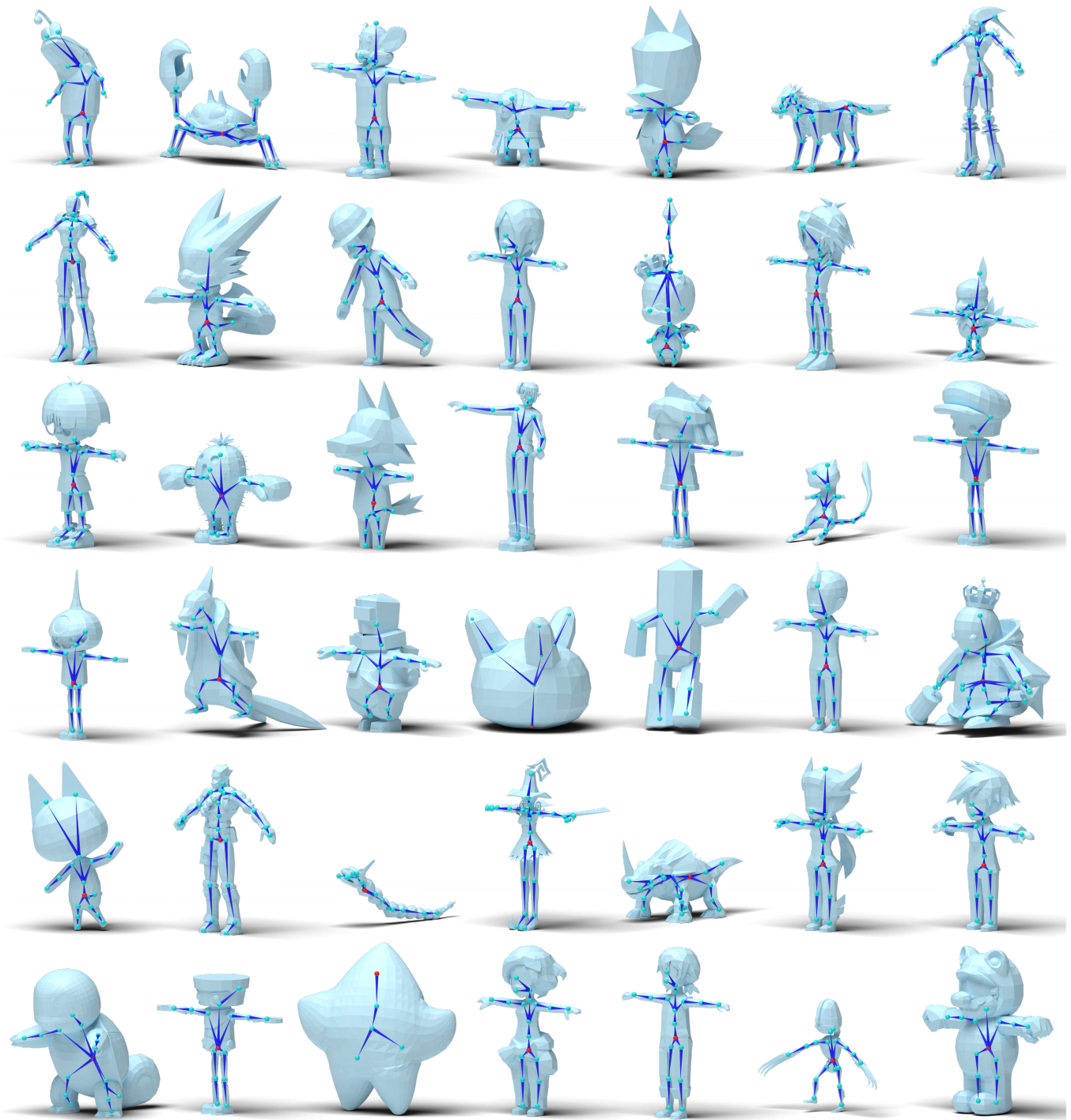


Figure 8: More results on the RigNet dataset. Please refer to the supplementary video for more 360-degree video results on both the RigNet and Objaverse dataset.

4.4 Ablation Study

We analyze various components of our method and compare their performance with the final model.

4.4.1 Joint Diffusion. In our full model, the joint diffusion module predicts the probability of the next joint position based on preceding joints in a skeleton sequence. This probabilistic approach effectively resolves structural ambiguities in skeleton tree representations, such as equivalent sibling node orderings, by accounting for their equivalence. In an ablation study, we replaced the joint diffusion loss with a deterministic L2 joint position loss. As shown in Fig. 6, using L2 loss leads to joints collapsing toward the middle axis, representing the mean position across samples due to sibling ambiguities within the skeleton sequence. In contrast, our method captures diverse joint position modalities, producing reasonable and accurate joint placements instead of averaged positions. Quantitative results in Tab. 4 further confirm that joint diffusion modeling significantly improves our method’s performance, boosting the skeleton IoU by almost two times.

Table 4: Ablation study results showing the impact of joint diffusion, normal injection, and pose augmentation on skeleton prediction.

| | IoU \uparrow | Prec. \uparrow | Rec. \uparrow | CD-J2J \downarrow | CD-J2B \downarrow | CD-B2B \downarrow |
|----------------------------|----------------|------------------|-----------------|---------------------|---------------------|---------------------|
| Ours w/o. joint diffusion | 0.308 | 0.277 | 0.364 | 0.068 | 0.059 | 0.046 |
| Ours w/o. injecting normal | 0.559 | 0.603 | 0.547 | 0.053 | 0.048 | 0.034 |
| Ours w/o. pose aug. | 0.741 | 0.768 | 0.732 | 0.037 | 0.037 | 0.022 |
| Ours full model | 0.765 | 0.786 | 0.765 | 0.033 | 0.034 | 0.019 |

4.4.2 Normal Injecting. To evaluate the impact of incorporating point normals into the shape tokens, we conducted a comparison experiment without point normals as input. The numerical results in Tab. 4 show a significant decline in skeleton performance when normal information is excluded, highlighting the importance of point normals as geometric information for improving performance.

4.4.3 Online Pose Augmentation. We analyze the effect of online data augmentation by randomly deforming input point clouds using the ground-truth skeleton and skinning. As shown in the numerical results in Sec. 4.4, pose augmentation improves skeleton prediction performance. Additionally, Fig. 6 compares results with and without pose augmentation on a character with a random skeleton pose not present in the dataset. Our full model generates a significantly better-aligned skeleton structure, whereas the model trained without pose augmentation fails to produce skeletons aligned with the shape and generates excessive joints. This augmentation enhances our method’s ability to generalize to objects in diverse poses. Furthermore, as demonstrated in Fig. 7, our method achieves high-quality skeletons even when the input shapes are obtained from real-world data and the targets are in arbitrary poses.

5 Limitation and Future Work

Although our method can automatically rig a variety of objects, there are several limitations and potential avenues for future work. First, our current approach does not allow for control over the level of detail in the rigs. Specifically, artists may need varying levels of detail in different parts of an object to achieve different degrees of motion control. To get this feature, more detailed rigging data shall be collected to allow for finer rigging (e.g., head and hand area), and we can introduce a condition in the network to provide control over

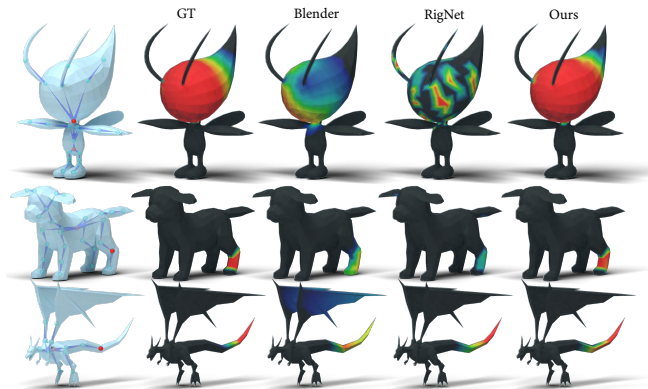


Figure 9: Comparison of skinning weight predictions. Our method produces more accurate and consistent weights, especially in challenging cases with large geodesic distances.

the level of detail. In addition, our method relies solely on geometry information to infer rigs, which can sometimes lack sufficient cues for the rig structure, leading to ambiguities. To improve this, texture information can be incorporated as an additional cue for automatic rigging in future iterations. Furthermore, our skinning weight prediction does not account for different motion styles, such as those influenced by materials. This limitation could be alleviated by incorporating dynamic data into the training process. However, high-quality dynamic data are scarce, and it would be interesting to explore the possibility of collecting such data to further improve rigging performance.

6 Conclusion

In this work, we present RigAnything, an autoregressive transformer-based method that automatically predicts rigs for 3D assets. To address the challenges posed by objects with diverse topologies and eliminate the inherent ambiguities in rigging, RigAnything probabilistically predicts the skeletons and assigns skinning weights, eliminating the need for any templates. This approach allows RigAnything to be trained end-to-end on both RigNet and the diverse Objaverse dataset, ensuring its versatility. Extensive experiments highlight the superiority of RigAnything across a wide range of object categories, showcasing its effectiveness and generalizability.

References

- Josh Achiam, Steven Adler, Sandhini Agarwal, Lama Ahmad, Ilge Akkaya, Florencia Leoni Aleman, Diogo Almeida, Janko Altschmidt, Sam Altman, Shyamal Anadkat, et al. 2023. Gpt-4 technical report. *arXiv preprint arXiv:2303.08774* (2023).
- Sherwin Bahmani, Ivan Skorokhodov, Victor Rong, Gordon Wetzstein, Leonidas Guibas, Peter Wonka, Sergey Tulyakov, Jeong Joon Park, Andrea Tagliasacchi, and David B Lindell. 2024. 4d-fy: Text-to-4d generation using hybrid score distillation sampling. In *Proceedings of the IEEE/CVF Conference on Computer Vision and Pattern Recognition*.
- Ilya Baran and Jovan Popović. 2007. Automatic rigging and animation of 3d characters. *ACM Transactions on graphics (TOG)* (2007).
- Tom Brown, Benjamin Mann, Nick Ryder, Melanie Subbiah, Jared D Kaplan, Prafulla Dhariwal, Arvind Neelakantan, Pranav Shyam, Girish Sastry, Amanda Askell, et al. 2020. Language models are few-shot learners. *Advances in neural information processing systems* (2020).
- Mark Chen, Alec Radford, Rewon Child, Jeffrey Wu, Heewoo Jun, David Luan, and Ilya Sutskever. 2020. Generative pretraining from pixels. In *International conference on machine learning*. PMLR, 1691–1703.

- An-Chieh Cheng, Xueting Li, Sifei Liu, Min Sun, and Ming-Hsuan Yang. 2022. Autoregressive 3d shape generation via canonical mapping. In *European Conference on Computer Vision*.
- Zedong Chu, Feng Xiong, Meiduo Liu, Jinzhi Zhang, Mingqi Shao, Zhaoxu Sun, Di Wang, and Mu Xu. 2024. HumanRig: Learning Automatic Rigging for Humanoid Character in a Large Scale Dataset. *arXiv preprint arXiv:2412.02317* (2024).
- Matt Deitke, Dustin Schwenk, Jordi Salvador, Luca Weihs, Oscar Michel, Eli VanderBilt, Ludwig Schmidt, Kiana Ehsani, Aniruddha Kembhavi, and Ali Farhadi. 2023. Objaverse: A universe of annotated 3d objects. In *Proceedings of the IEEE/CVF Conference on Computer Vision and Pattern Recognition*. 13142–13153.
- Prafulla Dhariwal and Alexander Nichol. 2021. Diffusion models beat gans on image synthesis. *Advances in neural information processing systems* 34 (2021), 8780–8794.
- Patrick Esser, Robin Rombach, and Bjorn Ommer. 2021. Taming transformers for high-resolution image synthesis. In *Proceedings of the IEEE/CVF conference on computer vision and pattern recognition*.
- Zhiyang Guo, Jinxu Xiang, Kai Ma, Wengang Zhou, Houqiang Li, and Ran Zhang. 2024. Make-It-Animatable: An Efficient Framework for Authoring Animation-Ready 3D Characters. *arXiv preprint arXiv:2411.18197* (2024).
- Bo Han, Hao Peng, Mingjing Dong, Yi Ren, Yixuan Shen, and Chang Xu. 2024. AMD: Autoregressive Motion Diffusion. In *Proceedings of the AAAI Conference on Artificial Intelligence*.
- Jonathan Ho, Ajay Jain, and Pieter Abbeel. 2020. Denoising diffusion probabilistic models. *Advances in neural information processing systems* 33 (2020), 6840–6851.
- Yicong Hong, Kai Zhang, Jiuxiang Gu, Sai Bi, Yang Zhou, Difan Liu, Feng Liu, Kalyan Sunkavalli, Trung Bui, and Hao Tan. 2023. Lrm: Large reconstruction model for single image to 3d. *arXiv preprint arXiv:2311.04400* (2023).
- Moritz Ibing, Gregor Kobsik, and Leif Kobbelt. 2023. Octree transformer: Autoregressive 3d shape generation on hierarchically structured sequences. In *Proceedings of the IEEE/CVF Conference on Computer Vision and Pattern Recognition*.
- Heewoo Jun and Alex Nichol. 2023. Shap-e: Generating conditional 3d implicit functions. *arXiv preprint arXiv:2305.02463* (2023).
- Jiahao Li, Hao Tan, Kai Zhang, Zexiang Xu, Fujun Luan, Yinghao Xu, Yicong Hong, Kalyan Sunkavalli, Greg Shakhnarovich, and Sai Bi. 2023. Instant3d: Fast text-to-3d with sparse-view generation and large reconstruction model. *arXiv preprint arXiv:2311.06214* (2023).
- Peizhuo Li, Kfir Aberman, Rana Hanocka, Libin Liu, Olga Sorkine-Hornung, and Baoquan Chen. 2021. Learning skeletal articulations with neural blend shapes. *ACM Transactions on Graphics (TOG)* (2021).
- Tianhong Li, Yonglong Tian, He Li, Mingyang Deng, and Kaiming He. 2024. Autoregressive Image Generation without Vector Quantization. *arXiv preprint arXiv:2406.11838* (2024).
- Isabella Liu, Hao Su, and Xiaolong Wang. 2024a. Dynamic Gaussians Mesh: Consistent Mesh Reconstruction from Monocular Videos. *arXiv preprint arXiv:2404.12379* (2024).
- Minghua Liu, Chao Xu, Haian Jin, Linghao Chen, Mukund Varma T, Zexiang Xu, and Hao Su. 2024b. One-2-3-45: Any single image to 3d mesh in 45 seconds without per-shape optimization. *Advances in Neural Information Processing Systems* (2024).
- Minghua Liu, Chong Zeng, Xinyue Wei, Ruoxi Shi, Linghao Chen, Chao Xu, Mengqi Zhang, Zhaoning Wang, Xiaoshuai Zhang, Isabella Liu, et al. 2024c. Meshformer: High-quality mesh generation with 3d-guided reconstruction model. *arXiv preprint arXiv:2408.10198* (2024).
- Ruoshi Liu, Rundi Wu, Basile Van Hoorick, Pavel Tokmakov, Sergey Zakharov, and Carl Vondrick. 2023. Zero-1-to-3: Zero-shot one image to 3d object. In *Proceedings of the IEEE/CVF international conference on computer vision*.
- Jing Ma and Dongliang Zhang. 2023. TARig: Adaptive template-aware neural rigging for humanoid characters. *Computers & Graphics* (2023).
- Paritosh Mittal, Yen-Chi Cheng, Maneesh Singh, and Shubham Tulsiani. 2022. Autosdf: Shape priors for 3d completion, reconstruction and generation. In *Proceedings of the IEEE/CVF Conference on Computer Vision and Pattern Recognition*.
- Alex Nichol, Heewoo Jun, Prafulla Dhariwal, Pamela Mishkin, and Mark Chen. 2022. Point-e: A system for generating 3d point clouds from complex prompts. *arXiv preprint arXiv:2212.08751* (2022).
- Alexander Quinn Nichol and Prafulla Dhariwal. 2021. Improved denoising diffusion probabilistic models. In *International conference on machine learning*. PMLR, 8162–8171.
- Niki Parmar, Ashish Vaswani, Jakob Uszkoreit, Lukasz Kaiser, Noam Shazeer, Alexander Ku, and Dustin Tran. 2018. Image transformer. In *International conference on machine learning*.
- William Peebles and Saining Xie. 2023. Scalable diffusion models with transformers. In *Proceedings of the IEEE/CVF International Conference on Computer Vision*. 4195–4205.
- Xuelin Qian, Yu Wang, Simian Luo, Yinda Zhang, Ying Tai, Zhenyu Zhang, Chengjie Wang, Xiangyang Xue, Bo Zhao, Tiejun Huang, et al. 2024. Pushing Auto-regressive Models for 3D Shape Generation at Capacity and Scalability. *arXiv preprint arXiv:2402.12225* (2024).
- Alec Radford, Jeffrey Wu, Rewon Child, David Luan, Dario Amodei, Ilya Sutskever, et al. 2019. Language models are unsupervised multitask learners. *OpenAI blog* (2019).
- Davis Rempe, Tolga Birdal, Aaron Hertzmann, Jimei Yang, Srinath Sridhar, and Leonidas J Guibas. 2021. Humor: 3d human motion model for robust pose estimation. In *Proceedings of the IEEE/CVF international conference on computer vision*. 11488–11499.
- Jiawei Ren, Liang Pan, Jiayang Tang, Chi Zhang, Ang Cao, Gang Zeng, and Ziwei Liu. 2023. Dreamgaussian4d: Generative 4d gaussian splatting. *arXiv preprint arXiv:2312.17142* (2023).
- Yichun Shi, Peng Wang, Jianglong Ye, Mai Long, Kejie Li, and Xiao Yang. 2023. Mv-dream: Multi-view diffusion for 3d generation. *arXiv preprint arXiv:2308.16512* (2023).
- Uriel Singer, Shelly Sheynin, Adam Polyak, Oron Ashual, Iurii Makarov, Filippos Kokkinos, Naman Goyal, Andrea Vedaldi, Devi Parikh, Justin Johnson, et al. 2023. Text-to-4d dynamic scene generation. *arXiv preprint arXiv:2301.11280* (2023).
- A Waswani, N Shazeer, N Parmar, J Uszkoreit, L Jones, A Gomez, L Kaiser, and I Polosukhin. 2017. Attention is all you need. In *Advances in Neural Information Processing Systems*.
- Yinghao Xu, Hao Tan, Fujun Luan, Sai Bi, Peng Wang, Jiahao Li, Zifan Shi, Kalyan Sunkavalli, Gordon Wetzstein, Zexiang Xu, et al. 2023. Dmv3d: Denoising multi-view diffusion using 3d large reconstruction model. *arXiv preprint arXiv:2311.09217* (2023).
- Zhan Xu, Yang Zhou, Evangelos Kalogerakis, Chris Landreth, and Karan Singh. 2020. Rignet: Neural rigging for articulated characters. *arXiv preprint arXiv:2005.00559* (2020).
- Xingguang Yan, Liqiang Lin, Niloy J Mitra, Dani Lischinski, Daniel Cohen-Or, and Hui Huang. 2022. Shapeformer: Transformer-based shape completion via sparse representation. In *Proceedings of the IEEE/CVF Conference on Computer Vision and Pattern Recognition*.
- Yuyang Yin, DeJia Xu, Zhangyang Wang, Yao Zhao, and Yunchao Wei. 2023. 4dgen: Grounded 4d content generation with spatial-temporal consistency. *arXiv preprint arXiv:2312.17225* (2023).
- Jianrong Zhang, Yangsong Zhang, Xiaodong Cun, Yong Zhang, Hongwei Zhao, Hongtao Lu, Xi Shen, and Ying Shan. 2023. Generating human motion from textual descriptions with discrete representations. In *Proceedings of the IEEE/CVF conference on computer vision and pattern recognition*.
- Kai Zhang, Sai Bi, Hao Tan, Yuanbo Xiangli, Nanxuan Zhao, Kalyan Sunkavalli, and Zexiang Xu. 2025. Gs-lrm: Large reconstruction model for 3d gaussian splatting. In *European Conference on Computer Vision*. Springer, 1–19.
- Yuyang Zhao, Zhiwen Yan, Enze Xie, Lanqing Hong, Zhenguo Li, and Gim Hee Lee. 2023. Animate124: Animating one image to 4d dynamic scene. *arXiv preprint arXiv:2311.14603* (2023).

A Final Training Objective

We train our entire model end-to-end, ensuring that joint positions, connectivity, and skinning weights are learned in a mutually reinforcing manner. Specifically, we combine the losses from the joint diffusion, connectivity, and skinning prediction modules into a single objective. The integrated objective allows the network to learn coherent skeleton structures and accurate skinning assignments simultaneously.

$$\mathcal{L} = \mathcal{L}_{\text{joint}} + \mathcal{L}_{\text{connect}} + \mathcal{L}_{\text{skinning}}.$$

B Skeleton Ambiguity

We elaborate on the two types of skeleton ambiguity introduced in the main paper, *i.e.*, the sibling ambiguity and the topology ambiguity. During the BFS ordering process used to traverse and sequentialize the skeleton tree, the ordering of nodes at the same depth in the BFS tree remains undefined. This can lead to the sibling ambiguity, as illustrated in Fig. 10. For example, when the preceding skeleton tokens are 1, 2, and 3, the next joint could either be 4 or 5, each with an equal probability of occurrence. Additionally, an object can have multiple valid skeleton topologies, as shown in Fig. 11, and the model must be capable of capturing these multiple valid configurations. Our method naturally addresses these by modeling the distribution of the next joint based on preceding predictions, which offers a distinct advantage over deterministic approaches in capturing the inherent uncertainty in joint positions.

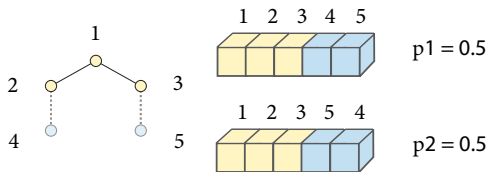


Figure 10: Illustration of sibling ambiguity during BFS ordering in skeletons.

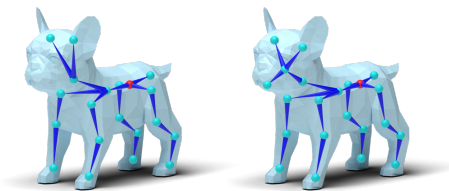


Figure 11: Two skeleton examples with different skeleton topologies generated on the same shape input.

C Dataset Details

Our dataset consists of a total of 12,040 shapes, combining 2,354 samples from the RigNet dataset and 9,686 shapes from the Objaverse dataset. From this collection, we utilize 11,217 samples for training and reserve 823 samples for validation and testing. The

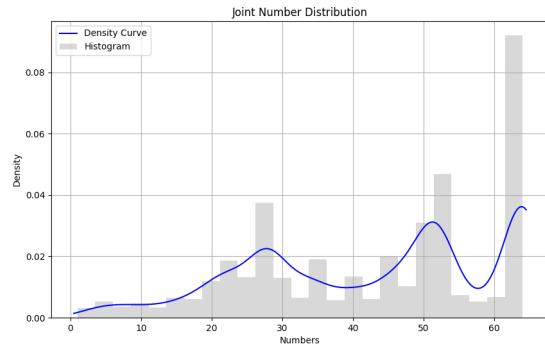


Figure 12: Distribution of joint numbers across shapes in our dataset.

dataset covers a wide range of object categories and poses, ensuring diversity and robustness in downstream tasks.

C.1 Data Filtering

We apply rigorous data filtering processes to ensure the quality and validity of the dataset. The filtering criteria differ slightly between the RigNet and Objaverse datasets due to their varying quality and size. For the RigNet dataset, which is already high-quality, we apply simple filtering based on the following principles:

- Shapes with more than 64 joints in their rigging are excluded.
- Shape are excluded if their skeleton is invalid (e.g. skeleton hierarchy does not form a proper tree structure).

For the Objaverse dataset, which is significantly larger, we employ both manual labeling and automated filtering scripts to ensure consistency and quality. The filtering is performed based on the following principles:

- Shapes with more than 64 joints in their rigging are excluded.
- Shapes are excluded if their skeleton is invalid (e.g. skeleton hierarchy does not form a proper tree structure).
- Shapes are excluded if the skeleton does not properly align with the corresponding geometry.
- Overly simplified or indistinguishable shapes (*i.e.* shapes consisting of only a few vertices and faces) are excluded.

The Objaverse dataset originally includes 21,622 shapes with rigging annotations. During filtering, we excluded 811 shapes with overly complicated skeletons containing more than 64 joints, which were usually associated with facial or hair rigs. Additionally, 10,471 shapes were filtered out due to low-quality rigging or skinning annotations, leaving us with a refined set of shapes with reliable rigging information.

C.2 Category statistics

For the Objaverse dataset, we also collect the Objaverse category labels and classify the shapes into six categories: humanoid/bipedal, quadruped, insectoid, avian, marine, and other. The "other" category typically includes manipulable articulated rigid objects found in the dataset (e.g. suitcases, cabinets, etc). Below, we provide the statistics for the number of shapes in each category in Tab. 5:

Table 5: Category statistics of the filtered Objaverse dataset.

| | Number |
|------------------|-------------|
| Humanoid/Bipedal | 7459 |
| Quadruped | 543 |
| Insectoid | 129 |
| Avian | 176 |
| Marine | 251 |
| Other | 830 |
| Total | 9388 |

C.3 Skeleton Distribution

We collect the distribution of joint numbers in each shape and provide the corresponding distribution plot below. Our dataset contains more shapes with joint numbers in the intervals $[25, 30]$, $[50, 55]$, and $[60, 64]$.